crystals

MDPI

Article

Gas Source Techniques for Molecular Beam Epitaxy of Highly Mismatched Ge Alloys

Chad A. Stephenson [1,*], Miriam Gillett-Kunnath [2], William A. O'Brien [3], Robert Kudrawiec [4] and Mark A. Wistey [1]

1 Department of Electrical Engineering, University of Notre Dame, Notre Dame, IN 46556, USA; mwistey@nd.edu
2 Department of Chemistry, Syracuse University, Syracuse, NY 13244, USA; miriam.kunnath@gmail.com
3 Rigetti Quantum Computing, 775 Heinz Avenue, Berkeley, CA 94710, USA; wobrien@rigetti.com
4 Faculty of Fundamental Problems of Technology, Wroclaw University of Science and Technology, Wybrzeze Wyspianskiego 27, 50-370 Wroclaw, Poland; robert.kudrawiec@pwr.edu.pl
* Correspondence: cstephe3@nd.edu; Tel.: +1-574-631-1290; Fax: +1-574-631-4393

Academic Editor: Paul J. Simmonds
Received: 21 October 2016; Accepted: 21 November 2016; Published: 2 December 2016

Abstract: Ge and its alloys are attractive candidates for a laser compatible with silicon integrated circuits. Dilute germanium carbide ($Ge_{1-x}C_x$) offers a particularly interesting prospect. By using a precursor gas with a Ge_4C core, C can be preferentially incorporated in substitutional sites, suppressing interstitial and C cluster defects. We present a method of reproducible and upscalable gas synthesis of tetrakis(germyl)methane, or $(H_3Ge)_4C$, followed by the design of a hybrid gas/solid-source molecular beam epitaxy system and subsequent growth of defect-free $Ge_{1-x}C_x$ by molecular beam epitaxy (MBE). Secondary ion mass spectroscopy, transmission electron microscopy and contactless electroreflectance confirm the presence of carbon with very high crystal quality resulting in a decrease in the direct bandgap energy. This technique has broad applicability to growth of highly mismatched alloys by MBE.

Keywords: germanium; germanium carbide; molecular beam epitaxy

1. Introduction

Ge and its alloys have kindled great interest for faster field effect and tunneling transistors, and even more interest as the possible "holy grail" CMOS-compatible laser [1–6]. Tensile Ge and optically pumped $Ge_{1-x}Sn_x$ lasers have been demonstrated, but these showed very high thresholds due to adverse band structures [3,4,6]. Dilute germanium carbide ($Ge_{1-x}C_x$) with $x \approx 0.01$ has recently been predicted to show a strongly direct bandgap and favorable band alignments, with optical emission expected to rival that of III–V semiconductors [7]. However, past growth of $Ge_{1-x}C_x$ using typical crystal growth techniques produced graphitic clusters and numerous carbon–carbon point defects [8–11].

$Ge_{1-x}C_x$ is a highly mismatched alloy (HMA). C atoms are much smaller and more electronegative than their Ge host, analogous to N in GaAs. This has unusual effects on the band structure of the alloy. In particular, the virtual crystal approximation fails to predict semiconductor properties such as bandgap and band alignment. For example, one might expect alloying Ge with diamond (or GaAs with GaN) to increase the bandgap, but it instead decreases. This is often explained through a mechanism known as band anticrossing, in which C (or N) introduces an uncharged (isoelectronic) but localized impurity state above the conduction band edge [12]. The localized state hybridizes with the conduction band states and pushes them lower into the bandgap. Remarkably, the interaction is significantly stronger at the direct bandgap at Γ ($k = 0$) than in the indirect valleys in Ge, which leads to the creation of a direct bandgap from two indirect bandgap materials.

Highly mismatched alloys (HMA) are, by definition, far from thermodynamic equilibrium and can be challenging to grow without segregation or other defects. For example, the *bulk* solubility of N in GaAs is only 10^{14} cm^{-3}, and C in Ge may be as low as 10^{8} cm^{-3} [13]. However, molecular beam epitaxy (MBE) is generally a kinetically limited process that can bypass thermodynamic limits and can incorporate several percent of the mismatched element [9,14]. Even so, HMAs must avoid high energy processes such as sputtering, implantation, and plasma ions to prevent segregation and formation of point defects [15]. Furthermore, $Ge_{1-x}C_x$ growth must avoid carbon–carbon bonds, which create midgap traps [16]. Therefore, successful growth of $Ge_{1-x}C_x$ must prevent C from remaining exposed on or segregating to the growth surface, leading to C clusters. Figure 1 shows the growth process using the chosen precursor gas method of tetrakis(germyl)methane (4GeMe).

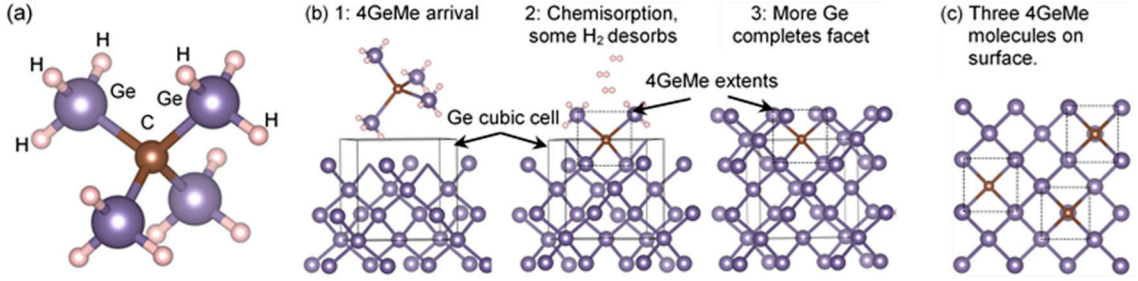

Figure 1. (**a**) 4GeMe molecule; (**b**) Steps of 4GeMe+Ge growth mechanism, in cross section (looking slightly off-axis). Ge cubic unit cell drawn for reference. The 4GeMe arrives as a "brick" and does not move; filling of the facet is done by GeH_x overpressure or by new Ge atoms after hydrogenation; (**c**) Parallel projection top view showing closest possible Ge_4C cores on a surface. C atoms are, at nearest, third-nearest neighbors, a stable state.

In this work, we present techniques for MBE of $Ge_{1-x}C_x$ without detectable carbon–carbon defects. Part 2 describes the synthesis of our carbon precursor gas source, 4GeMe, including modifications to the previous reports of the synthesis. Undesirable carbon–carbon bonds are avoided using a carbon precursor based on a Ge_4C core, in which each carbon atom is already fully surrounded by Ge [17,18]. This is distinct from the more common methylgermanes with Ge surrounded by multiple C atoms. Part 3 describes the hybrid gas source/solid source MBE system used for growth, and the techniques used. Part 4 describes our growth results. The pre-engineering of the desired final crystal structure by a priori precursor design is applicable to a range of material problems, and increases the value of epitaxy.

2. Synthesis of 4GeMe

The choice of carbon precursor gas was motivated by the possibility of depositing carbon fully surrounded by Ge atoms, greatly reducing the risk of forming undesirable carbon–carbon bonds at the surface. Thermal dehydrogenation of the tetra-substituted E_4C core in $(H_3E)_4C$ (E = Si, Ge; see Figure 1) precursors was reported for $Si_{1-x-y}Ge_xC_y$ alloys with bandgaps larger or smaller than $Si_{1-x}Ge_x$ [18–26]. The authors noted that these systems demonstrated a non-typical elongated Si–C and Ge–C bond length of 7% (1.89 Å (β-SiC)) and 5% (2.05 Å), respectively. This resulted in (i) the stretching of the E–C bonds to possibly reduce lattice strain and (ii) novel heteroatomic tetrels. E_4C compounds with a Ge_4C core could enable growth of dilute germanium carbide semiconductors with fully substitutional (sp^3) carbon in a diamond lattice. This could yield lasers and modulators that are compatible with conventional silicon chip fabrication [20,26–33].

The modified techniques presented here led to a high purity, reproducible, and up-scalable synthetic route to the family of germyl methanes including $(Cl_2BrGe)_4C$, (**1**), $(H_3Ge)_2CH_2$, (**2**), $(H_3Ge)_3CH$, (**3**), and $(H_3Ge)_4C$, the desired precursor (4GeMe, **4**). We confirm by multiple techniques that the correct nuclear magnetic resonance (NMR) spectra are different from published reports.

All manipulations were carried out under ultrahigh purity nitrogen or argon gas using Schlenk-line and glovebox techniques. Toluene and diethyl ether were dried over a copper-based catalyst and 4 Å molecular sieve columns (Innovative Technology, Newburyport, MA, USA). $GeCl_2$•dioxane, squalene, benzyltrimethyl ammonium chloride, $C_6H_5CH_2N(Cl)(CH_3)_3$, and 4N grade CBr_4, all anhydrous compounds from Sigma-Aldrich, were used as received. $LiAlH_4$ (anhydrous, Sigma-Aldrich, St. Louis, MO, USA), was recrystallized from diethyl ether.

2.1. Synthesis Procedures

The first step of synthesis was similar to [18], producing **$(Cl_2BrGe)_4C$ (1)** as follows. A Schlenk flask was charged with a 0.24 g (0.73 mmol) of CBr_4, 8 mL of toluene and a stir bar resulting in a clear and colorless solution. A separate flask was charged with 0.6 g (2.8 mmol) of $GeCl_2$.dioxane, 15–20 mL of toluene and a stir bar resulting in a colloidal white suspension. The solution of CBr_4 was slowly added to the latter via a stainless steel cannula. The mixture was then stirred for 2–12 h at room temperature resulting in a white cloudy solution. The reaction was then heated slowly to 80 °C, held at 80 °C for two hours, then filtered hot, resulting in a clear, colorless solution via a filter cannula. (Yield: 95%, or 85% scaled up five-fold.) All volatiles were evacuated off resulting in long thin white needles. Crystals of **1** were dissolved in dimethylformamide (DMF) and confirmed via electrospray mass spectroscopy (ESMS) in the positive-ion mode. The following ions were observed in positive-ion mode, (m/z): $CCl_{11}Ge_4^+$ (691), $CBrCl_{10}Ge_4^+$ (737), $CBr_2C_{l9}Ge_4^+$ (781), $CBr_3C_{l8}Ge_4^+$ (825), and $CBr_4C_{l7}Ge_4^+$ (870).

The second synthesis step produced multiple germyl methane groups **$(H_3Ge)_2CH_2$, (2), $(H_3Ge)_3CH$, (3), and $(H_3Ge)_4C$ (4GeMe, 4)**. A Schlenk flask was charged with 0.412 g (0.455 mmol) of compound **1**, 0.104 g (2.735 mmol) of $LiAlH_4$, 0.015 g (0.064 mmol) of $C_6H_5CH_2N(Cl)(CH_3)_3$, 15–20 mL of squalene and a large magnetic stir bar. The cloudy white mixture was stirred for 5 days at room temperature resulting in a light cream color. The reaction was heated for 2 h at 80 °C and then distilled for 12 h into a flask at −196 °C until a pale green color was seen (yields: 35%). This resulted in 4GeMe. A further distillation of the pale green compound at 80 °C for another 12 h into a separate flask at −196 °C resulted in a mixture of compounds **2** and **3**. To further increase the purity of 4GeMe, a four trap-to-trap distillation apparatus connected via high vacuum tubing was used to separate the distillates at various temperatures: (i) −45 °C, least volatile 4GeMe; (ii) −78 °C, compound **3**; (iii) −116 °C, compound **2**; and (iv) −196 °C for any unidentified side products. C_6D_6 (δ, ppm): **2**: GeH_3, t, 3.64; CH, sept, −0.20; **3**: GeH_3, d, 3.84; CH, quint, −0.60; 4GeMe: GeH_3, s, 3.34.

2.2. Synthesis Results and Discussion

Electrospray mass spectra (ESMS) in positive ion mode were recorded on a Micromass Quattro-LC triple quadrupole mass spectrometer with 100 °C source temperature, 125 °C desolvation temperature, 2.5 kV capillary voltage, and 20–55 V cone voltage [34]. The samples were introduced by direct infusion with a Harvard syringe pump at 10 µL/min. Gas Phase FT-IR was carried out on a Bruker Tensor 27 (Bruker, Billerica, MA, USA) spectrometer using a Pike Tech 10 cm gas cell with KBr windows. 1D and 2D NMR were carried out for ^1H, and $^{13}C\{^1H\}$ using 2D homonuclear correlation spectroscopy (COSY) [35], and ^{13}C-HMBC [36,37] on either a Bruker Avance III HD 400 (Bruker, Billerica, MA, USA) 400 MHz or a Varian DirectDrive 600 (Varian/Agilent, Santa Clara, CA, USA) 600 MHz spectrometer with C_6D_6 (δ (ppm): ^1H, 7.15; ^{13}C, 128.0) and $CDCl_3$ (δ (ppm): ^1H, 7.26; ^{13}C, 77.36) standards in an airtight J-tap NMR tube.

The initial synthesis step is readily achieved as the commercially available $GeCl_2$•dioxane undergoes a germylene insertion when reacted with carbon tetrabromide: $GeCl_2$•dioxane + CBr_4 → $(Cl_2BrGe)_4C$ (**1**) in a solution of toluene [18,19]. Previous reports indicated an initial reaction time of two hours at a 2.2 mmolar scale at room temperature with 79% yield [19]. In this work, a time study showed that slowly stirring for 8–12 h leads to almost complete conversion with 95% yield at a 2.2 mmolar scale, and 85% yield at a five-fold scale (see Table 1).

Additionally, if stringent air-free conditions and freshly distilled and degassed solvents are used, after filtering hot, pure large white needles grow immediately upon slow evacuation of all volatiles. This procedure eliminated the need for recrystallization. The ^{13}C spectrum showed no carbon peaks, as expected, as no traces of the starting material CBr_4 (C_6D_6, δ (ppm): s, −29.71) [38,39] or residual solvent peaks (toluene, C_6D_6, δ (ppm): CH_3, 21.10; C(*i*) 137.91; CH(*o*) 129.33; CH(*m*) 128.56; CH(*p*) 125.68) were detected [40]. We believe the increase in reaction time and slow evacuation of volatiles promotes complete germylene insertion without decomposition.

Table 1. Yields of $(Cl_2BrGe)_4C$ (**1**) and 4GeMe (**4**).

Compound	Yields			
$(Cl_2BrGe)_4C$	79% [a]	95% [b]	85% [c]	
$(H_3Ge)_4C$	0 [d]	0 [e]	0 [f]	35% [g]

[a] Repeated literature synthesis [18]: 2.2 mmol, rt, 2 h; [b] 2.2 mmol, rt, 8–12 h; [c] Five-fold increase of [b]; [d] repeated literature synthesis [18]: $LiAlH_4$, rt, 3d, then distillation at 60 °C for 8 h; [e] $LiAlH_4$, rt/40/50 °C, 2d/3d/5d, then distillation at 40/60/80 °C for 6/8/12 h; [f] $LiAlH_4$, rt, 3d, then distillation at 190–220 °C for 8–24 h; [g] $LiAlH_4$, rt, 3–5d, heat for 2 h at 80 °C, then distillation at 80 °C for 8–12 h.

To examine the stability of the Ge–C core, crystals of **1** were dissolved in a solution of DMF, and ESMS clearly showed that the sp^3 hybridized carbon cluster core remained intact even after ionization (see Figure 2). In the positive ion mode, several cluster species were characterized by their isotope pattern [18,19,34,41,42]. The clusters retained the mass of the core Ge_4C with several halides (m/z = $CCl_{11}Ge_4^+$ (691), $CBrCl_{10}Ge_4^+$ (737), $CBr_2Cl_9Ge_4^+$ (781), $CBr_3Cl_8Ge_4^+$ (825), and $CBr_4Cl_7Ge_4^+$ (870)), thus supporting the stability of compound **1**. Such multi metal-chalcogenide clusters, with partial oxidation caused by the electric ESMS field, is a common phenomenon when being ionized [41,42]. However, evidence of the intact core was unexpected as the Ge–Cl (356 kJ/mol) and Ge–Br (276 kJ/mol) have stronger bond dissociation energies than the Ge–C (255 kJ/mol) bond. Hence, one might expect the weaker Ge–C bonds to break apart first and fewer intact polyanions of compound **1** to be detected in the ESMS, but this did not occur [43–45]. This is a key point for epitaxial semiconductor growth using 4GeMe, since it suggests the C–Ge bonds can remain intact when the molecule adsorbs onto a Ge surface, especially if the strong halide bonds are replaced by weakly bonded hydrogen to create 4GeMe.

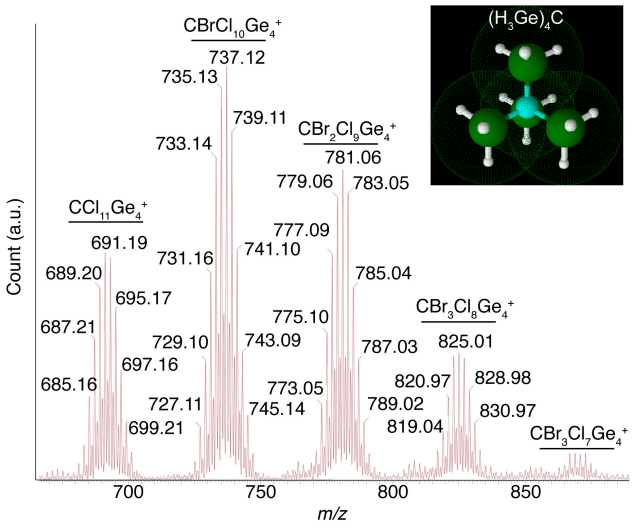

Figure 2. Electrospray mass spectra (ESMS) of synthesized 4GeMe showing the stability of the sp^3 core. Inset: 3D generated image of $(H_3E)_4C$ (E = Si, Ge). Atom colors: E = green, C = cyan, H = white.

These results confirmed that the tetrasubstituted sp^3 hybridized carbon core in **1** remains intact and could be reduced to produce the target compound, $(H_3Ge)_4C$, containing weaker Ge–H (290 kJ/mol vs. Ge–Cl 356 kJ/mol) bonds. In addition, this supports our hypothesis that it may be feasible that upon thermal dehydrogenation of the latter compound—4GeMe—the Ge_4C carbon core will remain intact. Moreover, the central carbon atom is also sterically protected by the bulky germanium atoms as in compound **1** (covalent radii: C = 0.77 Å, Ge = 1.22 Å) [43] (see Figure 2) thus assisting in driving the dissociation of the stronger Ge–H bonds [18]. Indeed, this is the case for hydrogermolysis reactions where the stronger terminal Ge–H bond in R_3Ge–H (R = Ph, Me) is cleaved at slightly elevated temperatures in preference to the weaker Ge–C bonds forming a Ge–Ge bond (256 kJ/mol) in R_3Ge–GeR'_3 (R = Ph, R′ = Et, Bu, Ph; R = Me, R′ = Bu) [34,46,47]. Hence, we proceeded in attempting to reproduce the syntheses of $(H_3Ge)_4C$ by utilizing lithium aluminium hydride to hydrogenate 4GeMe.

Several initial attempts at the reaction of **1** with anhydrous $LiAlH_4$ at the suggested [18] ambient temperatures for 3 days in a solvent with a high boiling point, such as squalene, followed by distillation (60 °C) were unsuccessful. At low temperatures, the synthesis did not proceed, and only a grey-white mixture was seen. Stirring for 1–10 days at higher temperatures from 60 to 220 °C was also not successful. An increase in temperatures concomitantly with longer reaction times instead led to the decomposition of the reaction mixture to unidentifiable dark brown-black solutions and precipitates (see Table 1 for more details).

A breakthrough was reached after numerous temperature vs. time reaction conditions were monitored over a period of five to ten days consecutively. As the reaction was stirred for a minimum of two days to a maximum of five days (neither increasing the yield of the target compound $(H_3Ge)_4C$ (4GeMe)), the color changed from a dark grey-white suspension to a pale cream color. At this stage, the reaction was heated over several hours to 80 °C and held there for 2 h. The reaction mixture was then distilled into a −196 °C trap for eight to twelve hours until a mint green color was seen.

A combination of clear liquid and waxy product, as expected [18,19], was collected along with a white precipitate. A gas phase FT-IR of the products showed positive indications of the target compound, 4GeMe, as the spectrum clearly showed the vibrational hydride, GeH_3, at 2075 cm^{-1} (vs., GeH str) and 839 cm^{-1} (m, GeH_3, sym def), along with CH vibrations at 3032 cm^{-1} (vw, CH str). This suggested that there were mixed products in the sample, possibly including partially hydrogenated compounds such as $(H_3Ge)_2CH_2$, (**2**) and $(H_3Ge)_3CH$, (**3**), along with the fully hydrogenated target compound, $(H_3Ge)_4C$, (4GeMe).

Thus, a ^1H NMR of the sample was taken in an airtight J-tap tube in C_6D_6 (see Figure 3). This showed several unidentified products, possibly including partially hydrogenated compounds and decomposition species. Nevertheless, the spectrum clearly shows peaks that are readily assigned to compound **2** (GeH_3, t, 3.64 ppm; CH, sept, −0.20 ppm) and compound **3** (GeH_3, d, 3.84 ppm; CH, dect., −0.60 ppm), in good agreement with [18]. However, the ^1H singlet (GeH_3) reported to be 4.07 ppm for 4GeMe was instead found at 3.34 ppm. This disparity may explain why other attempts to reproduce the synthesis technique in Ref. [18] were elusive. Extensive 2D experiments, below, were repeated to confirm that the GeH_3 shifts are at 3.34 ppm rather than the reported 4.07 ppm [18,19].

The 2D COSY spectrum in Figure 4A shows that the ^1H resonance signal at 3.84 ppm (green) correlates to the decatet at −0.60 ppm (green) and the resonance signal at 3.64 ppm (blue) correlates to septet at −0.20 ppm (blue), confirming that, indeed, compounds **2** and **3** exist, respectively. Also, the signal at 3.34 ppm correlates to no other signal, as expected for a singlet peak. In other words, all H atoms are in equivalent chemical environments, which is strong evidence for the desired target **4**, $(H_3Ge)_4C$.

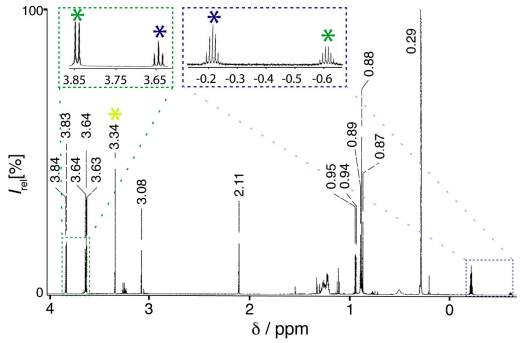

Figure 3. ^{1}H NMR from the mother liquor of the gas phase reaction collected in one trap at −196 °C. Contamination at this stage can be clearly identified (unstarred peaks). Compounds $(H_3Ge)_2CH_2$, **2** (**blue** *); $(H_3Ge)_3CH$, **3** (**green** *), and $(H_3Ge)_4C$ (4GeMe, **yellow** *) are initially identified with their splitting pattern.

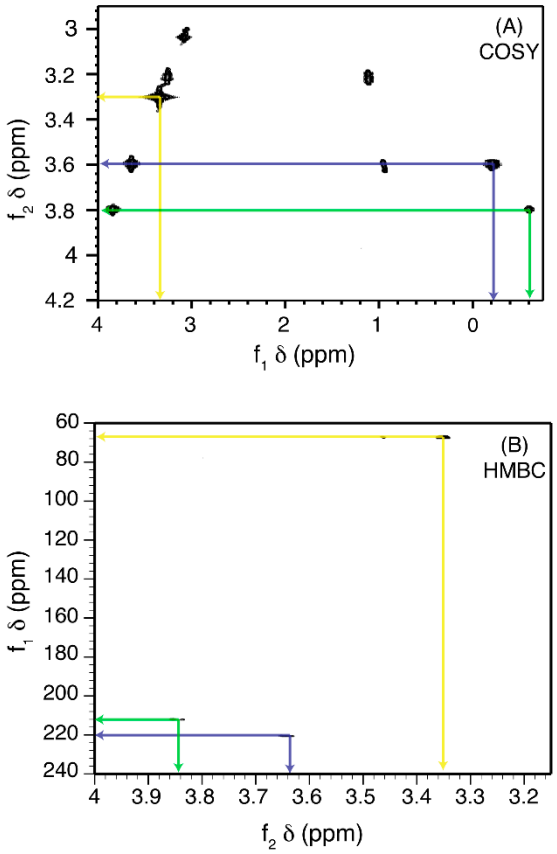

Figure 4. (**A**) 2D **^{1}H** COSY shows coupling of the protons; (**B**) 2D **^{1}H-^{13}C** HMBC shows correlation of the protons two bonds away (i.e., GeH_3) to the carbon core in compounds **2** (**blue** *); **3** (**green** *); and 4GeMe (**yellow** *). Lines are guides to the eye.

In Figure 4B, 2D HMBC correlates the resonance signal of the central carbon atom core with the resonance of the proton through C–Ge–H bonding. This would be detected if, indeed, a proton is two bonds away from carbon, hence confirming the hydrogenation product and stability of the compound in C_6D_6 at room temperature conditions. Compounds **2** (**blue** *), **3** (**green** *), and 4GeMe (**yellow** *) correlate a proton triplet at 3.63 ppm to the carbon signal at 220.55 ppm in compound **2**, $(H_3Ge)_2CH_2$; a proton doublet at 3.83 ppm to the carbon signal at 211.92 ppm in compound **3**, $(H_3Ge)_3CH$; and a proton singlet at 3.342 ppm to the carbon signal at 67.37 ppm in compound

4GeMe, $(H_3Ge)_4C$. Hence, this reaction pathway was clearly a one-pot synthesis for all three of these compounds.

Fractional distillation was used to separate the products, keeping **2** and **3** as these have been shown to dramatically improve the growth of germanium on silicon wafers [31,48–50]. Thus, a four trap-to-trap distillation apparatus connected via high vacuum tubing collected the distillates from the reaction vessel at various temperatures: (i) −45 °C for the least volatile 4GeMe; (ii) −78 °C for **3**; (iii) −116 °C for **2**; and (iv) −196 °C for any unidentified side products. Compounds **2** and **3** were isolated at said temperatures as seen via NMR, as previously discussed. However, in the first trap, we were able to isolate 4GeMe free of contaminants (see Figure 5) except for the partially hydrogenated $(H_3Ge)_2CBr_2$ species. For this compound, ^{1}H singlet at 2.114 ppm correlated with ^{13}C signal at 21.4 ppm in HMBC spectrum [51]. Although not 100% pure, this is a significant improvement from the previous sample (refer to Figure 3), and the remaining background compound is not expected to interfere with semiconductor growth [17].

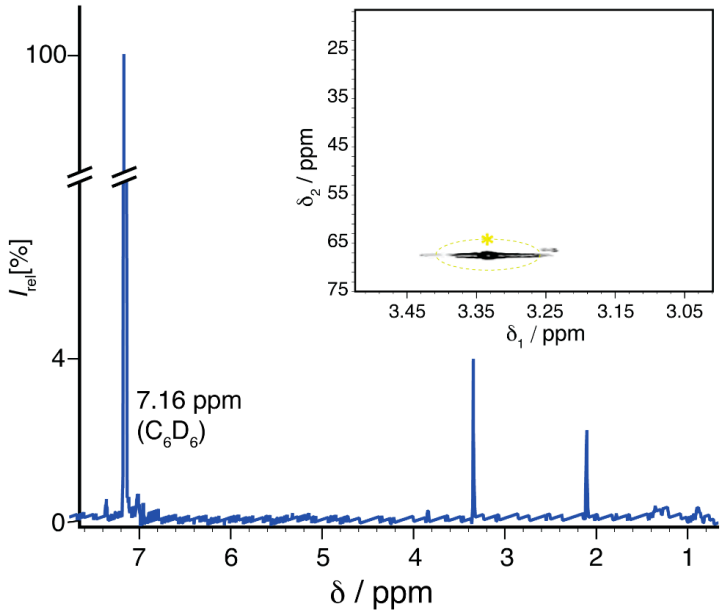

Figure 5. ^{1}H NMR of a sample collected at −48 °C showing a drastically cleaner sample of compound $(H_3Ge)_4C$, (4GeMe, marked with **yellow** *); the peak at 2.114 ppm corresponds to $(H_3Ge)_2CBr_2$, which is the only remaining contaminant in the sample and benign for growth. This signal correlates with the carbon signal at 21.4 ppm in the corresponding HMBC spectrum. Inset: HMBC spectrum for 4GeMe.

3. Growth System and Techniques

With the desired 4GeMe precursor in hand, we turned to epitaxial growth. For MBE of $Ge_{1-x}C_x$, we designed a gas delivery system attached to an Intevac Mod Gen II MBE to perform hybrid gas-source/solid-source growth, particularly of Group IV materials. The growth chamber is pumped by a corrosive-rated Pfeiffer 1200 °C turbomolecular pump as well as an ion pump. A substrate manipulator capable of reaching 1200 °C for desorbing suboxides from silicon wafers was installed, although the growths presented here were performed on GaAs substrates. A Staib reflection high energy electron diffraction (RHEED) gun with a differential pumping option allows operation at high chamber pressures, although differential pumping has not been found to be necessary in growths to date. The MBE has a background pressure of 6×10^{-10} Torr without liquid nitrogen (LN2), and $<1 \times 10^{-10}$ Torr with LN2.

The gas delivery system in Figure 6 was designed to allow maximum flexibility in the growth of different materials, with digermane, trisilane, and additional ports for custom precursor gases such

as $(H_3Ge)_4C$ or dopants. Gas pressures are measured using Baratron gauges (MKS, Orland Park, IL, USA) for true gas pressure independent of species. Also, unlike thermocouple or Pirani gauges with hot (80–120 °C) wires, Baratrons operate at low ambient temperatures that avoid precracking of any delicate precursors (e.g., SnD_4). The gas flow is accurately and precisely controlled to extremely low flow rates through either Horiba Z500 (Horiba, Boulder, CO, USA) digital mass flow controllers or computer-controlled leak valves. A residual gas analyzer (RGA) allows in situ sampling of the precursor gases within the gas cabinet, as well as leak checking, before opening to the MBE chamber. Four capacitive manometers provide a true measure of pressure independent of gas species [52]. Gases are delivered to the growth chamber by either a cold injector or hot injector, allowing the freedom to use multiple gases simultaneously, including gases that require pre-cracking prior to their arrival at the wafer surface and those that do not. The gas delivery system was designed with minimal dead space to reduce memory effects and increase gas switching speeds. All valves and mass flow controllers (MFCs) are under computer control, and every gas inlet has at least two paths to each MBE gas injector line.

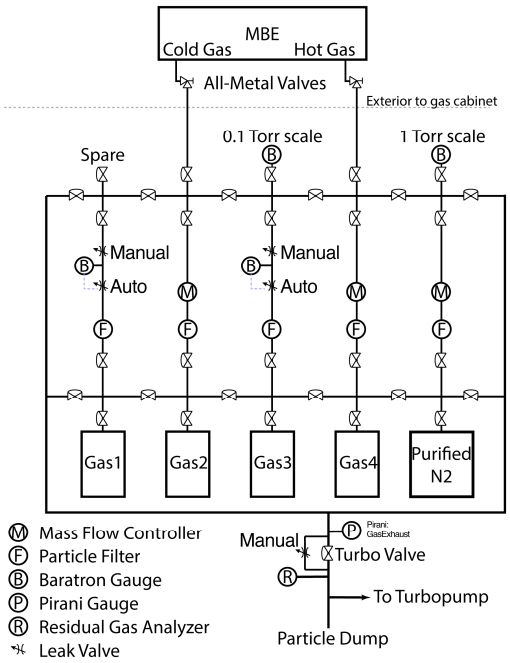

Figure 6. Gas cabinet layout.

Initial gas-source growths of Ge using digermane showed that the gas utilization was very weak, with <0.1% incorporation. We determined the original cold gas injector nozzle was too far from the surface of the wafer, leading to significant overspray. We replaced the injector with a single 6 mm outer diameter stainless steel tube ending 10 cm from the wafer center. In addition, the majority of the precursor gas that failed to adhere to the wafer surface subsequently condensed on the nearby MBE cryoshroud, which is cooled by liquid nitrogen and has a significantly larger surface area. Although this eliminated the typical memory effect seen in gas source growths, it also prevented any opportunity for additional adsorption attempts of gas molecules with the wafer surface. Therefore, the LN_2 was turned off for gas source growths and was found to be unnecessary due to the low background pressure in the MBE chamber.

4. Growth Method

In order to provide carrier confinement and optical transparency at the relevant wavelengths near the Ge band edge, growth was performed on GaAs(100) substrates. The initial III–V buffer growth was completed on a GaAs(100) wafer in a Veeco Gen 930 III–V MBE chamber (Veeco, St. Paul, MN,

USA), which is attached under ultrahigh vacuum (UHV) to the hybrid source MBE mentioned above. The native oxide was desorbed under As beam equivalent pressure (BEP) of 1×10^{-5} Torr, then a clean epitaxial surface was grown with a 100 nm GaAs buffer, a 50 nm AlAs layer as a back barrier, and another 20 nm of GaAs. Sample flatness was confirmed by a streaky RHEED pattern. The sample was then transferred under UHV to the hybrid source MBE chamber.

As mentioned above, carbon–carbon bonds must be prevented from forming during $Ge_{1-x}C_x$ growth to avoid midgap trap states [16]. Common carbon sources for epitaxial growth, such as CBr_4, metalorganics, and plasmas, all deposit bare C atoms on the Ge surface, and these atoms ride the growth front until they meet other C atoms and incorporate as carbon clusters [10,53–55]. Worse yet, hyperthermal C and hot graphite evaporate directly as large clusters of carbon atoms (C_8 and larger) [10], forming unavoidable defects in Ge. In contrast, by using $(H_3Ge)_4C$, the carbon atom is fully surrounded by Ge, with no C–H bonds and no direct way for C to bond to a surface. Even if two $(H_3Ge)_4C$ molecules land side by side, the C atoms are no closer than third-nearest neighbors, which is a known stable crystal structure [56].

When using the 4GeMe molecule, the growth temperature has to be optimized so that the Ge–H bonds can thermally crack but the Ge–C bond does not. Solid-source Ge and digermane allow for high quality crystal growth at lower temperatures than the commonly used germane gas. However, if the growth is at too low of a temperature, crystal originated pits will form due to the formation of Ge vacancies. Conversely, too high of a growth temperature will break Ge–C bonds in the 4GeMe, and C atoms will be exposed to form undesirable C clusters.

The Group IV growth began with 10 nm of solid-source Ge grown at 400 °C (thermocouple) at a growth rate of 60 nm/h. For the remainder of the growth, the Ge shutter was left open. In order to maximize the 4GeMe incorporation efficiency, the ion pump remained off during the growth, and the gate valve was closed to the turbomolecular pump. The 4GeMe was then injected at a foreline pressure of 30 mTorr as measured on the capacitive manometer for 20 s, at which point the growth chamber pressure had risen to 5×10^{-5} Torr by ion gauge. The gate valve was left closed for an additional 40 s to allow the 4GeMe additional residence time in the chamber, while solid source Ge continued to deposit. Next, the gate valve was opened for 20 s to pump out the residual gases. This 4GeMe deposition was repeated for a total of 15 cycles (20 min), for a total of 20 nm of solid-source Ge growth. The substrate temperature was increased by 25 °C, then 50 nm of solid-source Ge was grown. This cycle was repeated a total of six times, with successively higher substrate temperatures up to 525 °C.

5. Experimental Results

Figure 7 shows the cross-sectional transmission electron microscopy of the Ge:C sample. The first several layers of Ge and Ge:C appear to have grown smoothly. The growth appears to turn rough above 475 °C. It is important to note that C clusters can act as Frank-Read sources, which would generate large dislocation networks, but analysis of the TEM shows no signs of dislocations. Figure 8 shows secondary ion mass spectroscopy (SIMS) performed on the sample by Evans Analytical Group, showing clear C incorporation. It appears that at the lower growth temperatures there is incomplete incorporation of the 4GeMe molecule. At 450 °C and above, the incorporation increases, suggesting more complete cracking and/or adsorption (sticking coefficient) of 4GeMe. The plateaus seen in Figure 8 are at approximately 0.03% and 0.05%. Due to the roughness of the sample and the limited resolution of SIMS, the C content is effectively averaged over the entire Ge and $Ge_{1-x}C_x$ superlattice and does not directly measure the C in the quantum wells. Considering the thicknesses of the 20 nm $Ge_{1-x}C_x$ wells and 50 nm Ge barrier layers, the 0.05% average is equivalent to approximately 0.2% C in the $Ge_{1-x}C_x$ wells grown at $T_{sub} \geq 450$ °C.

To look for subtle changes in the direct bandgap, contactless electroreflectance (CER) measurements were performed. Like photoreflectance (PR), CER modulates the built-in electric field in the sample, which changes the reflectance at energies corresponding to direct optical transitions such as the direct bandgap [57,58]. An important advantage of CER over PR spectroscopy is the elimination

of problems with the modulation of the refractive index inside the sample which leads to an unwanted Fabry–Perot oscillation [59]. A strong direct bandgap transition followed by Franz–Keldysh oscillations (FKO) is visible in the CER spectrum of the Ge:C sample shown in Figure 9. The transition energy can be estimated from the analysis of FKO [60] as shown in the inset in Figure 9.

Despite the very small amount of C shown in SIMS, Figure 9 shows a decrease in the direct bandgap energy from 0.80 eV (Ge) to 0.776 eV, a difference of 24 meV. To the authors' knowledge, this was the first demonstration of a decrease in direct bandgap in a Ge:C sample with no defects detectable by electron-dispersive X-ray spectroscopy in scanning transmission electron microscopy (STEM-EDX), nuclear reaction analysis Rutherford backscattering spectroscopy (NRA-RBS), or Raman spectroscopy [17]. It is noteworthy that a significant reduction in direct bandgap was achieved even though the carbon and defect concentrations were both below the detectable limits of these common techniques.

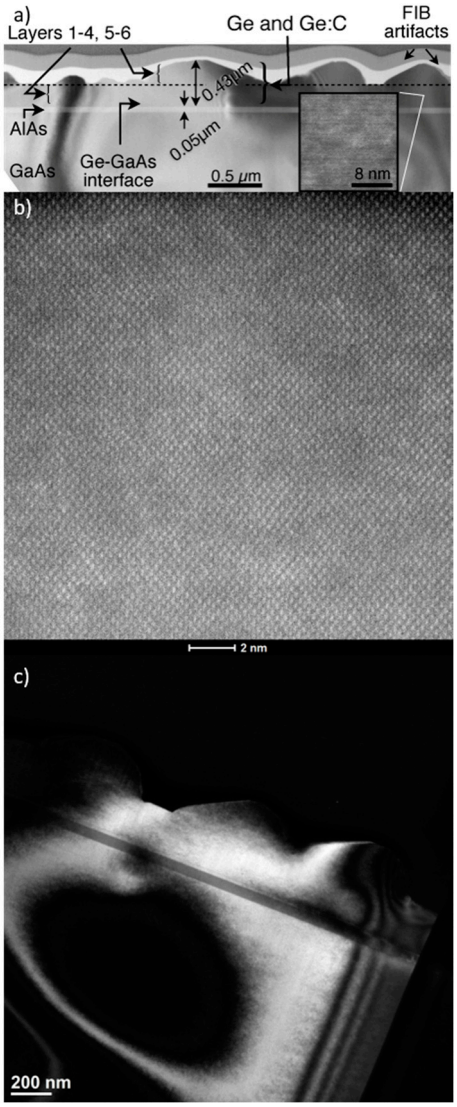

Figure 7. (**a**) Bright-field TEM of $Ge_{1-x}C_x$ growth on AlAs/GaAs. Inset: HRTEM of location indicated; (**b**) STEM across a $Ge_{1-x}C_x$ layer shows high crystallinity with no apparent segregation; (**c**) Dark field g = (0 0 −4) TEM shows no dislocations nucleating from any $Ge_{1-x}C_x$ layer. Reproduced with permission from [Stephenson], [*J. Appl. Phys.*]; published by [AIP], [2016].

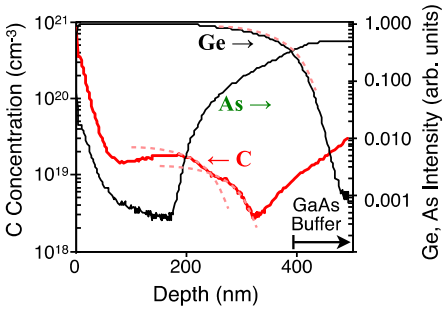

Figure 8. SIMS of Ge:C growth on AlAs/GaAs. Two plateaus in C are visible. To aid extraction of C despite smearing due to rough surface, dashed lines are copies of the Ge concentration profile near the Ge/GaAs interface, as shown with an additional dashed curve for Ge. Reproduced with permission from [Stephenson], [*J. Appl. Phys.*]; published by [AIP], [2016].

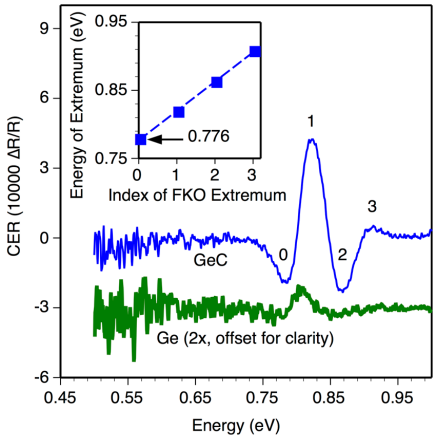

Figure 9. Room temperature CER spectrum of the Ge:C sample: a direct bandgap transition followed by FKO is clearly visible. Inset: FKO peak/valley positions (squares) with linear fit (dashed) extrapolated to direct bandgap (n = 0).

6. Discussion

Bare C atoms on the surface can ride the growth front, which is a longstanding problem in this material system. When C atoms ride the surface, they incorporate into the growth when they meet additional C atoms and form C–C or larger carbon clusters. As shown in Figure 7, crystal quality is very high with no stacking faults or dislocations detected. Another confirmation of the crystal quality is the lack of detectable carbon clusters by HRTEM, Raman spectroscopy, and NRA-RBS [17]. Due to the lack of evidence of C clusters, it is believed that the C atoms are incorporating as part of the Ge_4C structure of the original $(H_3Ge)_4C$ molecule. There was a distinct change in growth kinetics above 475 °C, which the authors attribute to chemisorption of the $(H_3Ge)_4C$ leading to a H_2-passivated surface. Further growths are required to identify growth conditions for flat layers; however, SIMS suggests that 450 °C is needed for complete $(H_3Ge)_4C$ incorporation while keeping below 475 °C for smooth growth.

The clear CER signal observed in Figure 9 shows very good crystallinity with a strong direct optical transition at the Γ point of the Brillouin zone. A decrease in the direct bandgap of 24 meV is consistent with theoretical predictions and very close to the photoreflectance results [17]. Additional growth with %C close to 1 at % should be performed to confirm the theoretical predictions for a direct bandgap and confirm the measured decrease in bandgap is due to C and not the Franz–Keldysh effect.

A 1:100 ratio for $(H_3Ge)_4C$ Ge BEP was chosen in order to grow dilute $Ge_{1-x}C_x$ with <1 at % C. Our initial growth assumed that the sensitivities would be similar, and choosing a BEP for $(H_3Ge)_4C$

that was approximately one percent of Ge's BEP would give a reasonable incorporation rate. However, when comparing relative sensitivity factors (R_g) for different atoms and molecules, assuming it can be approximated by the ratio of ionization cross sections at 150 eV [61], a Ge_2H_6 molecule is expected to have an R_g approximately double that of GeH. The R_g for $Si(CH_3)_4$ is nearly four times that of GeH [62]. We attribute the difference between $(H_3Ge)_4C$:Ge fluxes and C:Ge atomic mole fractions to the difference in R_g between our Ge source and $(H_3Ge)_4C$. Although the ionization cross section and sensitivity factor of $(H_3Ge)_4C$ are unknown, a factor of 5 difference fits the trend for GeH_3, GeH_4, and Ge_2H_6.

Mass transport calculations are as follows. Molecular flow through 1.4 m of tubing with an inner diameter of 4.6 mm from the foreline to the delivery end of the gas injector, the gas conductivity of the gas delivery line is $C_{pipe,mol} = \bar{c}\pi d^3 l^{-1}/12 = 2.6$ mL/s [63]. For a foreline pressure of 30 mTorr, this corresponds to a flow of 7.8×10^{-5} Torr L·s^{-1}.

One of the challenges to producing direct bandgap GeSn and related alloys is the strain present in the materials. In order to turn Ge into a direct bandgap semiconductor, 1.4%–2% biaxial strain must be applied [2,64–67]. A direct bandgap GeSn laser was recently demonstrated, but that required >12% Sn [6]. To grow a direct bandgap, $Ge_{1-x}C_x$ should require less than 1% C [7]. The People–Bean model [68] predicts a critical thickness of 1250 nm for 1% C $Ge_{1-x}C_x$ on Ge, so strain does not limit Ge:C device design. This contrasts with GeSn, where it predicts 57 nm critical thickness. Even the more conservative Matthews–Blakeslee model predicts a $Ge_{1-x}C_x$ critical thickness of 36 nm, which is more than enough thickness for quantum wells [69]. What little strain does exist in Ge:C is tensile, which contributes favorably, if negligibly, to a direct bandgap.

7. Conclusions

Through the use of specially designed precursor gases and a custom designed gas delivery system, molecular beam epitaxy is uniquely capable of growing HMAs like $Ge_{1-x}C_x$ well into the miscibility gap. Taking advantage of kinetically-limited growth regimes, C can be effectively incorporated without defects. When incorporated substitutionally, contactless electroreflectance confirms a decrease in direct bandgap with very dilute amounts of C in Ge.

Acknowledgments: We gratefully acknowledge support from the National Science Foundation (DMR-1508646 and CBET-1438608), the Semiconductor Research Corporation Nanoelectronics Research Initiative, and the National Institute of Standards and Technology through the Midwest Institute of Nanoelectronics Discovery (MIND). We also thank the Notre Dame Center for Environmental Science & Technology (CEST) and Jesse Tice for their timely advice and knowledge, Sergei Rouvimov and the Notre Dame Integrated Imaging Facility (NDIIF), and Jaroslav Zajicek for his helpful discussions. Additional support was provided by the Center for Sustainable Energy at Notre Dame through use of the Materials Characterization Facility (MCF) and the ND Energy Postdoctoral Fellowship Program.

Author Contributions: Chad A. Stephenson, William A. O'Brien, and Mark A. Wistey conceived and designed the MBE growth experiments; Miriam Gillett-Kunnath performed the chemical synthesis; Chad A. Stephenson and William A. O'Brien performed the growth experiments; Robert Kudrawiec provided CER data and analysis; Chad A. Stephenson and Mark A. Wistey wrote the paper.

Conflicts of Interest: The authors declare no conflict of interest.

References

1. Nam, D.; Sukhdeo, D.; Cheng, S.-L.; Roy, A.; Chih-Yao Huang, K.; Brongersma, M.; Nishi, Y.; Saraswat, K. Electroluminescence from strained germanium membranes and implications for an efficient Si-compatible laser. *Appl. Phys. Lett.* **2012**, *100*, 131112. [CrossRef]
2. De Kersauson, M.; El Kurdi, M.; David, S.; Checoury, X.; Fishman, G.; Sauvage, S.; Jakomin, R.; Beaudoin, G.; Sagnes, I.; Boucaud, P. Optical gain in single tensile-strained germanium photonic wire. *Opt. Express* **2011**, *19*, 17925–17934. [CrossRef] [PubMed]
3. Liu, J.; Sun, X.; Camacho-Aguilera, R.; Kimerling, L.C.; Michel, J. Ge-on-Si laser operating at room temperature. *Opt. Lett.* **2010**, *35*, 679–681. [CrossRef] [PubMed]

4. Camacho-Aguilera, R.E.; Cai, Y.; Patel, N.; Bessette, J.T.; Romagnoli, M.; Kimerling, L.C.; Michel, J. An electrically pumped germanium laser. *Opt. Express* **2012**, *20*, 11316–11320. [CrossRef] [PubMed]
5. Gupta, S.; Magyari-Köpe, B.; Nishi, Y.; Saraswat, K.C. Achieving direct band gap in germanium through integration of Sn alloying and external strain. *J. Appl. Phys.* **2013**, *113*, 53707. [CrossRef]
6. Wirths, S.; Geiger, R.; von den Driesch, N.; Mussler, G.; Stoica, T.; Mantl, S.; Ikonic, Z.; Luysberg, M.; Chiussi, S.; Hartmann, J.M.; et al. Lasing in direct-bandgap GeSn alloy grown on Si. *Nat. Photonics* **2015**, *9*, 88–92. [CrossRef]
7. Stephenson, C.A.; O'brien, W.A.; Qi, M.; Penninger, M.; Schneider, W.F.; Wistey, M.A. Band Anticrossing in Dilute Germanium Carbides Using Hybrid Density Functionals. *J. Electron. Mater.* **2015**, *45*, 2121–2126. [CrossRef]
8. D'Arcy-Gall, J.; Gall, D.; Petrov, I.; Desjardins, P.; Greene, J.E. Quantitative C lattice site distributions in epitaxial $Ge_{1-y}C_y$/Ge(001) layers. *J. Appl. Phys.* **2001**, *90*, 3910–3918. [CrossRef]
9. Kolodzey, J.; Berger, P.R.; Orner, B.A.; Hits, D.; Chen, F.; Khan, A.; Shao, X.; Waite, M.M.; Ismat Shah, S.; Swann, C.P.; et al. Optical and electronic properties of SiGeC alloys grown on Si substrates. *J. Cryst. Growth* **1995**, *157*, 386–391. [CrossRef]
10. Steele, W.C.; Bourgelas, F.N. Studies of Graphite Vaporization Using a Modulated Beam Mass Spectrometer. Air Force Materials Laboratory, Technical Report AFML-TR-72-222. 1972. Available online: http://www.dtic.mil/dtic/tr/fulltext/u2/755899.pdf (accessed on 22 November 2016).
11. Park, S.Y.; D'Arcy-Gall, J.; Gall, D.; Kim, Y.-W.; Desjardins, P.; Greene, J.E. C lattice site distributions in metastable $Ge_{1-y}C_y$ alloys grown on Ge(001) by molecular-beam epitaxy. *J. Appl. Phys.* **2002**, *91*, 3644–3652. [CrossRef]
12. Shan, W.; Walukiewicz, W.; Ager, J.W., III; Haller, E.E.; Geisz, J.F.; Friedman, D.J.; Olson, J.M.; Kurtz, S.R. Band anticrossing in GaInNAs alloys. *Phys. Rev. Lett.* **1999**, *82*, 1221–1224. [CrossRef]
13. Scace, R.I.; Slack, G.A. Solubility of Carbon in Silicon and Germanium. *J. Chem. Phys.* **1959**, *30*, 1551–1555. [CrossRef]
14. Zhang, S.B.; Wei, S.H. Nitrogen solubility and induced defect complexes in epitaxial GaAs:N. *Phys. Rev. Lett.* **2001**, *86*, 1789–1792. [CrossRef] [PubMed]
15. Wistey, M.A.; Bank, S.R.; Yuen, H.B.; Bae, H.; Harris, J.S. Nitrogen plasma optimization for high-quality dilute nitrides. *J. Cryst. Growth* **2005**, *278*, 229–233. [CrossRef]
16. Gall, D.; D'Arcy-Gall, J.; Greene, J.E. C incorporation in epitaxial $Ge_{1-y}C_y$ layers grown on Ge (001): An ab initio study. *Phys. Rev. B* **2000**, *62*, 7723–7726. [CrossRef]
17. Stephenson, C.A.; O'Brien, W.A.; Penninger, M.W.; Schneider, W.F.; Gillett-Kunnath, M.; Zajicek, J.; Yu, K.M.; Kudrawiec, R.; Stillwell, R.A.; Wistey, M.A. Band structure of germanium carbides for direct bandgap silicon photonics. *J. Appl. Phys.* **2016**, *120*, 053102. [CrossRef]
18. Kouvetakis, J.; Haaland, A.; Shorokhov, D.J.; Volden, H.V.; Girichev, G.V.; Sokolov, V.I.; Matsunaga, P. Novel Methods for CVD of Ge_4C and $(Ge_4C)_xSi_y$ Diamond-like Semiconductor Heterostructures: Synthetic Pathways and Structures of Trigermyl-$(GeH_3)_3CH$ and Tetragermyl-$(GeH_3)_4C$ Methanes. *J. Am. Chem. Soc.* **1998**, *7863*, 6738–6744. [CrossRef]
19. Matsunaga, P.T.; Kouvetakis, J.; Groy, T.L. Synthesis and Characterization of Tetrakis(trihalogermyl)methanes. Molecules Containing Sterically Strained Carbon Centers. *Inorg. Chem.* **1995**, *34*, 5103–5104. [CrossRef]
20. Kouvetakis, J.; Todd, M.; Chandrasekhar, D.; Smith, D.J. Novel chemical routes to silicon-germanium-carbon materials. *Appl. Phys. Lett.* **1994**, *65*, 2960–2962. [CrossRef]
21. Todd, M.; Matsunaga, P.; Kouvetakis, J.; Chandrasekhar, D.; Smith, D.J. Growth of heteroepitaxial $Si_{1-x-y}Ge_xC_y$ alloys on silicon using novel deposition chemistry. *Appl. Phys. Lett.* **1995**, *67*, 1247–1249. [CrossRef]
22. Kouvetakis, J.; Nesting, D.; Keeffe, M.O.; Smith, D.J. Ordered Structures in Unstrained, Epitaxial Ge–Si–C Films. *Chem. Mater.* **1998**, *4756*, 1396–1401. [CrossRef]
23. Kouvetakis, J.; Chandrasekhar, D.; Smith, D.J. Growth and characterization of thin $Si_{80}C_{20}$ films based upon Si_4C building blocks. *Appl. Phys. Lett.* **1998**, *72*, 930–932. [CrossRef]
24. Rücker, H.; Methfessel, M.; Bugiel, E.; Osten, H. Strain-stabilized highly concentrated pseudomorphic $Si_{1-x}C_x$ layers in Si. *Phys. Rev. Lett.* **1994**, *72*, 3578–3581. [CrossRef] [PubMed]
25. Hoffmann, L.; Bach, J.C.; Bech Nielsen, B.; Leary, P.; Jones, R.; Öberg, S. Substitutional carbon in germanium. *Phys. Rev. B* **1997**, *55*, 11167–11173. [CrossRef]

26. Ohfuti, M.; Sugiyama, Y.; Awano, Y.; Yokoyama, N. Electronic structure of $Si_{1-y}C_y$ and $Si_{1-x-y}Ge_xC_y$ alloys with low C concentrations. *Phys. Rev. B* **2001**, *63*, 195202. [CrossRef]
27. Osten, H.; Bugiel, E.; Zaumseil, P. Growth of an inverse tetragonal distorted SiGe layer on Si (001) by adding small amounts of carbon. *Appl. Phys. Lett.* **1994**, *64*, 3440–3442. [CrossRef]
28. Krishnamurthy, M.; Drucker, J.S.; Challa, A. Epitaxial growth and characterization of $Ge_{1-x}C_x$ alloys on Si(100). *J. Appl. Phys.* **1995**, *78*, 7070–7073. [CrossRef]
29. Kolodzey, J.; O'Neil, P.A.; Zhang, S.; Orner, B.A.; Roe, K.; Unruh, K.M.; Swann, C.P.; Waite, M.M.; Shah, S.I. Growth of germanium-carbon alloys on silicon substrates by molecular beam epitaxy. *Appl. Phys. Lett.* **1995**, *67*, 1865–1867. [CrossRef]
30. Todd, M.; Kouvetakis, J.; Smith, D.J. Synthesis and characterization of heteroepitaxial diamond-structured $Ge_{1-x}C_x$ (x = 1.5%–5.0%) alloys using chemical vapor deposition. *Appl. Phys. Lett.* **1996**, *68*, 2407–2409. [CrossRef]
31. Todd, M.; Mcmurran, J.; Kouvetakis, J.; Smith, D.J. Chemical Synthesis of Metastable Germanium—Carbon Alloys Grown Heteroepitaxially on (100) Si. *Chem. Mater.* **1996**, *4756*, 2491–2498. [CrossRef]
32. Soref, R.A. Optical band gap of the ternary semiconductor $Si_{1-x-y}Ge_xC_y$. *J. Appl. Phys.* **1991**, *70*, 2470–2472. [CrossRef]
33. Osten, H.; Barth, R.; Fischer, G.; Heinemann, B.; Knoll, D.; Lippert, G.; Rücker, H.; Schley, P.; Röpke, W. Carbon-containing group IV heterostructures on Si: Properties and device applications. *Thin Solid Films* **1998**, *321*, 11–14. [CrossRef]
34. Scientific Instrument Services. Isotope Distribution Calculator and Mass Spec Plotter. Available online: http://www.sisweb.com/mstools/isotope.htm (accessed on 21 November 2016).
35. Bax, A.; Griffey, R.H.; Hawkins, B.L. Correlation of proton and nitrogen-15 chemical shifts by multiple quantum NMR. *J. Magn. Reson.* **1983**, *55*, 301–315. [CrossRef]
36. Bax, A.; Summers, M.F. 1H and 13C Assignments from Sensitivity-Enhanced Detection of Heteronuclear Multiple-Bond Connectivity by 2D Multiple Quantum NMR. *J. Am. Chem. Soc.* **1986**, *108*, 2093–2094. [CrossRef]
37. Bax, A.; Subramanian, S. Sensitivity-enhanced two-dimensional heteronuclear shift correlation NMR spectroscopy. *J. Magn. Reson.* **1986**, *67*, 565–569. [CrossRef]
38. Cadogan, J.I.G.; Ley, S.V.; Patenden, G.; Raphael, R.A.; Rees, C.W. (Eds.) *Dictionary of Organic Compounds*, 6th ed.; Chapman & Hall Electron. Pub. Div.: London, UK, 1996.
39. Reich, H.J. C-13 Chemical Shifts. Available online: http://www.chem.wisc.edu/areas/reich/handouts/nmr-c13/cdata.htm (accessed on 21 November 2016).
40. Gottlieb, H.E.; Kotlyar, V.; Nudelman, A. NMR Chemical Shifts of Common Solvents as Trace Impurities. *J. Org. Chem.* **1997**, *62*, 7512–7515. [CrossRef] [PubMed]
41. Gaumet, J.-J.; Strouse, G.F. Electrospray Mass Spectrometry of Semiconductor Nanoclusters: Comparative Analysis of Positive and Negative Ion Mode. *J. Am. Soc. Mass Spectrom.* **2000**, *11*, 338–344. [CrossRef]
42. Gillett-Kunnath, M.M.; Petrov, I.; Sevov, S.C. Heteroatomic deltahedral zintl ions of group 14 and their alkenylation. *Inorg. Chem.* **2010**, *49*, 721–729. [CrossRef] [PubMed]
43. Cotton, F.A.; Wilkinson, G.; Murillo, C.A.; Bochmann, M. *Advanced Inorganic Chemistry*, 6th ed.; Wiley-Interscience: New York, NY, USA, 1999.
44. Buriak, J.M. Organometallic Chemistry on Silicon and Germanium Surface. *Chem. Rev.* **2002**, *102*, 1271–1308. [CrossRef] [PubMed]
45. Darwent, B.D. *Bond Dissociation Energies in Simple Molecules*; U.S. Government Printing Office Washington, D.C. 20402: Washington, DC, USA, 1970.
46. Subashi, E.; Rheingold, A.L.; Weinert, C.S. Preparation of oligogermanes via the hydrogermolysis reaction. *Organometallics* **2006**, *25*, 3211–3219. [CrossRef]
47. Amadoruge, M.L.; DiPasquale, A.G.; Rheingold, A.L.; Weinert, C.S. Hydrogermolysis reactions involving the α-germylated nitriles R_3GeCH_2CN (R=Ph, Pr^i, Bu^t) and germanium amides R_3GeNMe_2 (R=Pr^i, Bu^t) with Ph_3GeH: Substituent-dependent reactivity and crystal structures of $Pr^i{}_3GeGePh_3$ and $Bu^t{}_3Ge[NHC(CH_3)CHCN]$. *J. Organomet. Chem.* **2008**, *693*, 1771–1778. [CrossRef]
48. Kelly, D.Q.; Wiedmann, I.; Donnelly, J.P.; Joshi, S.V.; Dey, S.; Banerjee, S.K.; Garcia-Gutierrez, D.I.; José-Yacamán, M. Thin germanium-carbon alloy layers grown directly on silicon for metal-oxide-semiconductor device applications. *Appl. Phys. Lett.* **2006**, *88*, 152101. [CrossRef]

49. Wistey, M.A.; Fang, Y.-Y.; Tolle, J.; Chizmeshya, A.V.G.; Kouvetakis, J. Chemical routes to Ge/Si(100) structures for low temperature Si-based semiconductor applications. *Appl. Phys. Lett.* **2007**, *90*, 82108. [CrossRef]
50. Fang, Y.Y.; Tolle, J.; Tice, J.; Chizmeshya, A.V.G.; Kouvetakis, J.; D'Costa, V.R.; Menéndez, J. Epitaxy-driven synthesis of elemental Ge/Si strain-engineered materials and device structures via designer molecular chemistry. *Chem. Mater.* **2007**, *19*, 5910–5925. [CrossRef]
51. Silverstein, R.M.; Webster, F.X.; Kiemel, D.J. *Spectrometric Identification of Organic Compounds*, 7th ed.; Wiley-Interscience: New York, NY, USA, 2005.
52. Daudé, B.; Elandaloussi, H.; Janssen, C. On the gas dependence of thermal transpiration and a critical appraisal of correction methods for capacitive diaphragm gauges. *Vacuum* **2014**, *104*, 77–87. [CrossRef]
53. Kim, S.-I.; Kim, M.; Min, S. Strain and critical layer thickness analysis of carbon-doped GaAs. *Solid State Commun.* **1996**, *97*, 875–878. [CrossRef]
54. D'Arcy-Gall, J.; Desjardins, P.; Petrov, I.; Greene, J.E.; Paultre, J.-E.; Masut, R.A.; Gujrathi, S.C.; Roorda, S. Epitaxial metastable $Ge_{1-y}C_y$ ($y \leq 0.02$) alloys grown on Ge(001) from hyperthermal beams: C incorporation and lattice sites. *J. Appl. Phys.* **2000**, *88*, 96–104. [CrossRef]
55. Zavitsanos, P.D.; Carlson, G.A. Experimental study of the sublimation of graphite at high temperatures. *J. Chem. Phys.* **1973**, *59*, 2966–2973. [CrossRef]
56. Guedj, C.; Kolodzey, J.; Hairie, A. Structure and lattice dynamics of $Ge_{1-y}C_y$ alloys using anharmonic Keating modeling. *Phys. Rev. B* **1999**, *60*, 150–153. [CrossRef]
57. Dybała, F.; Zelazna, K.; Maczko, H.; Gladysiewicz, M.; Misiewicz, J.; Kudrawiec, R.; Lin, H.; Chen, R.; Shang, C.; Huo, Y.; et al. Electromodulation spectroscopy of direct optical transitions in $Ge_{1-x}Sn_x$ layers under hydrostatic pressure and built-in strain. *J. Appl. Phys.* **2016**, *119*, 215703. [CrossRef]
58. Kopaczek, J.; Polak, M.P.; Scharoch, P.; Wu, K.; Chen, B.; Tongay, S.; Kudrawiec, R. Direct optical transitions at K- and H-point of Brillouin zone in bulk MoS_2, $MoSe_2$, WS_2, and WSe_2. *J. Appl. Phys.* **2016**, *119*, 215703. [CrossRef]
59. Kudrawiec, R.; Sitarek, P.; Misiewicz, J.; Bank, S.R.; Yuen, H.B.; Wistey, M.A.; Harris, J.S. Interference effects in electromodulation spectroscopy applied to GaAs-based structures: A comparison of photoreflectance and contactless electroreflectance. *Appl. Phys. Lett.* **2005**, *86*, 1–3. [CrossRef]
60. Ishikawa, Y.; Wada, K.; Cannon, D.D.; Liu, J.; Luan, H.-C.; Kimerling, L.C. Strain-induced band gap shrinkage in Ge grown on Si substrate. *Appl. Phys. Lett.* **2003**, *82*, 2044–2406. [CrossRef]
61. Gas Correction Factors for Bayard-Alpert Ionization Gauges. Available online: http://www.thinksrs.com/downloads/PDFs/ApplicationNotes/IG1BAgasapp.pdf (accessed on 21 November 2016).
62. Ali, M.A.; Kim, Y.-K.; Hwang, W.; Weinberger, N.M.; Rudd, M.E. Electron-impact total ionization cross sections of silicon and germanium hydrides. *J. Chem. Phys.* **1997**, *106*, 9602–9608. [CrossRef]
63. Introduction to Vacuum Technology Fundamentals: Conductance. Available online: https://www.pfeiffer-vacuum.com/en/know-how/introduction-to-vacuum-technology/fundamentals/conductance/ (accessed on 21 November 2016).
64. Ishikawa, Y.; Wada, K. Germanium for silicon photonics. *Thin Solid Films* **2010**, *518*, S83–S87. [CrossRef]
65. Virgilio, M.; Manganelli, C.L.; Grosso, G.; Pizzi, G.; Capellini, G. Radiative recombination and optical gain spectra in biaxially strained n-type germanium. *Phys. Rev. B* **2013**, *87*, 235313. [CrossRef]
66. Hoshina, Y.; Iwasaki, K.; Yamada, A.; Konagai, M. First-Principles Analysis of Indirect-to-Direct Band Gap Transition of Ge under Tensile Strain. *Jpn. J. Appl. Phys.* **2009**, *48*, 04C125. [CrossRef]
67. Chang, G.-E.; Cheng, H.H. Optical gain of germanium infrared lasers on different crystal orientations. *J. Phys. D. Appl. Phys.* **2013**, *46*, 65103. [CrossRef]
68. People, R.; Bean, J.C. Calculation of critical layer thickness versus lattice mismatch for Ge_xSi_{1-x}/Si strained-layer heterostructures. *Appl. Phys. Lett.* **1985**, *47*, 322–324. [CrossRef]
69. Matthews, J.W.; Blakeslee, A.E. Defects in epitaxial multilayers. *J. Cryst. Growth* **1974**, *27*, 118–125. [CrossRef]